ARTICLES

Interligand Electron Transfer Dynamics in $[Os(bpy)_3]^{2+}$: Exploring the Excited State Potential Surfaces with Femtosecond Spectroscopy

George B. Shaw, David J. Styers-Barnett, Erika Z. Gannon, Jeremy C. Granger, and John M. Papanikolas*

Department of Chemistry, University of North Carolina at Chapel Hill,
Chapel Hill, North Carolina 27599-3290

Received: August 11, 2003; In Final Form: March 16, 2004

Femtosecond transient absorption studies of $[Os(bpy)_3]^{2+}$ have been performed to gain new insights into the excited-state dynamics. Experiments were performed for a series of excitation wavelengths throughout both the singlet and triplet metal-to-ligand charge transfer (MLCT) bands. The dynamics are probed via the $\pi-\pi^*$ transition on the bpy^- anion at 370 nm. Time scales for interligand electron transfer (ILET) and vibrational cooling are extracted from the amplitude and anisotropy of the excited state absorptions. The ILET rate has been measured as a function of temperature and, from these data, estimates for the electron transfer activation energy and ligand−ligand coupling are made. Our data also provide insight into the vibrational cooling dynamics within these large complexes, suggesting that vibrational cooling occurs only when exciting into the singlet MLCT state, after intersystem crossing. It appears that photoexcitation within the triplet MLCT absorption produces molecules that are vibrationally cold, even for excitation at the blue edge of the absorption band.

I. Introduction

The photophysics of Ru(II) and Os(II) polypyridine complexes have been studied for more than three decades.[1−9] The motivation for this research has largely been driven by the use of $[Ru(bpy)_3]^{2+}$ and $[Os(bpy)_3]^{2+}$ (bpy = 2,2′-bipyridine) and their derivatives as photosensitizers in the fields of solar energy conversion,[10−12] photonic devices,[13−15] and molecular electronics.[16,17] Through this extensive investigation, the properties of the lowest energy triplet metal-to-ligand charge-transfer (^{3}MLCT) excited state and its evolution at long times after photoexcitation have been well-characterized. Only recently, however, have significant strides been taken toward understanding the behavior of these complexes at very early times after photoexcitation. Following ^{1}MLCT excitation, intersystem crossing (ISC) to the triplet manifold is the dominant relaxation pathway (i.e. near unit efficiency) prior to ground-state recovery via phosphorescence. Recent ultrafast experiments have suggested that ISC occurs in $[Ru(bpy)_3]^{2+}$ within a few hundred femtoseconds after photoexcitation,[18,19] though certain aspects remain open to interpretation.[20]

Despite the recent advances made in developing a comprehensive picture of the evolution of the excited state from the moment of photoexcitation, certain fundamental questions remain largely unanswered. It is well-established that a polar solvent localizes the electron distribution on a single ligand at long times after photoexcitation.[21,22] Whether a localized or delocalized excited state is initially produced is still a matter of debate. In the last two decades, compelling arguments have been made for both cases,[23−33] mostly investigating Ru(II) compounds. Nevertheless, this debate continues. Recently, McCusker and co-workers studied $[Ru(bpy)_3]^{2+}$ in nitrile solvents using ultrafast absorption anisotropy measurements.[34] They proposed that photoexcitation produced an initially delocalized ^{1}MLCT state that quickly localized on a single ligand due to nondiffusive solvation dynamics.

A previous contribution from our laboratory[35] discussed femtosecond transient absorption and absorption anisotropy experiments that were used to investigate the excited-state dynamics in $[Os(bpy)_3]^{2+}$ and a mixed ligand Os(II) complex that has two bipyridine ligands and one amide functionalized bipyridine. In those experiments, the complexes were excited at the far red edge of the ground state absorption spectrum. This allowed us to populate the lowest optically accessible ^{3}MLCT state, and circumvent the ISC process. In $[Os(bpy)_3]^{2+}$, it was found that the photoexcited electron was able to incoherently hop among the three bipyridines with an interligand electron transfer (ILET) time of $\tau_{ILET} = 8.1$ ps. We also found evidence suggesting that the distribution of local solvent configurations at the instant of photoexcitation gave rise to a mixture of localized and delocalized excited states.

This paper describes several extensions to our initial work that enhance our understanding about the excited-state potential surfaces in polar solvents. Molecular dynamics simulations were carried out to gain quantitative insight into the heterogeneity of the solvent environment at the moment of photoexcitation. The results support our previous findings that there should be a mixture of localized and delocalized excited states due to this inhomogeneity. These simulations also strengthen the conclusions drawn from the optical studies described in the current

---

* Address correspondence to this author.E-mail: john_papanikolas@unc.edu.

10.1021/jp0363850 CCC: $27.50

work. We have measured the ILET rate constant as a function of temperature to determine the activation energy for electron transfer (850 cm^{-1}), and combined this with estimates of the reorganization energy to determine the ligand−ligand coupling (300−400 cm^{-1}). We have extended our ultrafast studies to other excitation wavelengths throughout the ^{1}MLCT and ^{3}MLCT absorption bands. These experiments explore higher energy portions of the excited-state potential surfaces, and provide insight into the partitioning of optical excitation energy between molecular vibrations (inner sphere) and solvent interactions (outer sphere). They indicate that the absorption spectra in polar solvents should be viewed, at least qualitatively, as overlapping absorption bands that correspond to the promotion of the electron to ligands whose energies are split by the inhomogeneous solvent environment. In short, excitation at the blue edge of the absorption band corresponds to promoting the system to an *upper* Marcus surface. Excitation into the ^{1}MLCT absorption band is followed by rapid intersystem crossing to form a vibrationally hot ^{3}MLCT state, which then cools with a time constant of 16 ps.

II. Experimental Section

The experimental apparatus has been described in detail elsewhere,[35,36] so only a brief description is provided here. The transient absorption spectrometer is based on a commercially available ultrafast laser system (Clark CPA-2001). Femtosecond pulses are produced by an erbium-doped fiber ring oscillator and injected into a chirped pulse Ti:sapphire regenerative amplifier. The amplifier, which is pumped by a frequency doubled, Q-switched Nd:YAG laser, produces 120 fs laser pulses at 775 nm at 1 kHz with pulse energies of approximately 950 μJ/pulse. The amplified output is split into two beams by an uncoated glass window.

The larger (96%) transmitted portion is directed into an optical parametric amplifier (OPA) where the tunable light used for photoexcitation is produced. For the ^{3}MLCT excitations the second harmonic of the OPA was used to generate light at 693, 675, 650, 625, and 580 nm with 5−10 μJ/pulse. The 500 nm excitation light (0.7 μJ/pulse) was generated by sum-frequency mixing of the fundamental at 1409 nm and the left over 775 nm light from the OPA, and the 440 nm excitation light was produced by fourth harmonic generation. For all excitation wavelengths, the pump was focused to a spot size of ~500 μm at the sample. The polarization of the pump beam was controlled with an achromatic $\lambda/2$ waveplate. To account for fluctuations in laser intensity during the course of data collection, after the sample the pump was directed into a photodiode whose voltage was continuously monitored for power normalization.

The probe beam is generated from the weak (4%) reflected fraction of the amplifier output that is directed into a corner retroreflector mounted on a computer-controlled translation stage. The beam is focused into a 6 mm thick CaF_2 window to generate a white light continuum that is then collimated by an achromatic lens. The continuum is attenuated and split into two beams of nearly equal intensity by taking the front and rear surface reflections from a 25 mm thick uncoated quartz window. The resulting beams are designated “signal” and “reference”. Both beams are focused by 300 mm lenses to have a 150 μm spot size at the sample. While both beams pass through the sample, only the signal beam is spatially overlapped at the sample with the pump beam. Both signal and reference beams are simultaneously directed into a 270 mm focal length spectrograph, dispersed by a 1200 line/mm holographic grating and detected by a 1024 × 256 pixel (25.4 × 6.35 mm) liquid nitrogen cooled CCD array. The spectrograph has a reciprocal linear dispersion of 3.1 nm/mm and the binning of the CCD has 128 pixels over the 25.4 mm dimension of the chip. Although we operate the device in a slit-less manner, the signal and reference beams are focused to a 0.5 mm spot at the entrance of the spectrograph—in essence, a virtual slit—resulting in a spectral resolution of 1.48 nm. The TA apparatus is capable of measuring a 77 nm segment of the transient absorption spectrum centered anywhere between 350 and 1000 nm with a sensitivity of better than 1 mOD.

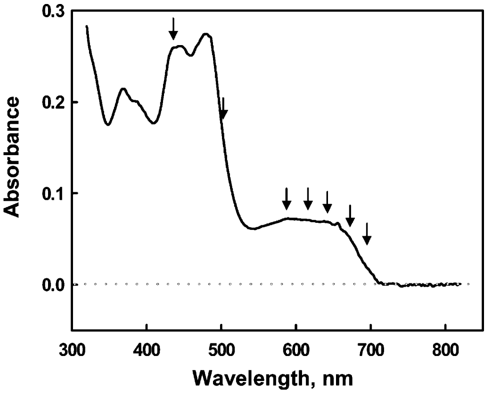

Figure 1. Ground-state absorption spectrum of $[Os(bpy)_3]^{2+}$. Photoexcitation wavelengths for TA experiments are indicated.

For the temperature-dependent studies, a home-built thermal regulator was designed. It consists of an aluminum block that was machined to accept our 2 mm path length sample cuvette and provide a small window to permit the pump, signal, and reference beams to pass through while ensuring maximum contact with the rest of the cuvette. Water (or a water/ethylene glycol mixture) pumped from a temperature-controlled circulating bath flows through channels machined in the aluminum block to maintain the temperature of the system. A thermocouple attached to the cuvette near where the laser beams pass through permits accurate measurement of the solution temperature. Sufficient time for thermal equilibration of the system was allowed before experiments were performed.

The $[Os(bpy)_3]^{2+}$ samples were obtained in crystal form (as PF_6^- salts) as gifts from Thomas J. Meyer and were used without further purification. Spectroscopic grade acetonitrile was used as obtained from the vendor (Burdick and Jackson). All experiments were performed on solutions whose concentrations were adjusted to give an optical density of ~0.3 OD in a 2 mm path length sample cell.

III. Results and Discussion

The ground-state absorption spectrum for $[Os(bpy)_3]^{2+}$ is shown in Figure 1. There are two relevant MLCT absorptions in the visible region: an intense singlet absorption band centered at 450 nm and a weaker triplet absorption extending from 520 to 700 nm. Photoexcitation to the ^{1}MLCT state is followed by rapid and efficient intersystem crossing to the ^{3}MLCT state manifold. This paper describes femtosecond transient absorption studies that probe the excited-state relaxation dynamics in $[Os(bpy)_3]^{2+}$ following photoexcitation at both singlet and triplet excitation wavelengths. Seven different photoexcitation wavelengths were used, and these are indicated by the arrows in Figure 1.

A. Molecular Dynamics Simulations of Solvent Inhomogeneity: Implications for the Optically Prepared Excited State. The degree of charge delocalization in the optically prepared MLCT state is determined by the relative magnitudes of the electronic coupling between the bipyridine ligands and the electrostatic asymmetry presented by the solvent environment. The electronic coupling mixes the π*-orbitals on the three ligands yielding a delocalized excited state. For an isolated molecule, or one embedded in a symmetric environment, the ligand orbitals are nearly degenerate and a weak electronic coupling is sufficient to achieve complete delocalization. The situation may be quite different for a complex embedded in a polar solvent. The electrostatic asymmetry presented by the local environment will lift the degeneracy of the three ligands, and if the asymmetry is large enough, the electronic states will have localized charge distributions. The degree of charge localization in the *optically prepared* state will depend on the solvent configuration surrounding the ground-state complex at the instant of photon absorption. Thus, the relevant question is: what is the distribution of solvent configurations that surround the *ground state* complex? The $[Os(bpy)_3]^{2+}$ ground state has no dipole moment and so (on average) it is surrounded by a symmetric electrostatic solvent environment. This should not be interpreted to imply that at the instant of photoexcitation all of the complexes in the ensemble experience a truly symmetric solvent environment, as the electrostatic field produced by the solvent cage surrounding the ground-state complex could possess a considerable amount of inhomogeneity. To address the question of environmental inhomogeneity, we have performed molecular dynamics simulations on a dipolar solvent interacting with the electronic ground state of $[Os(bpy)_3]^{2+}$.

The computer model consists of a transition metal complex surrounded by 504 dipolar solvent molecules. The potential was composed of two parts, i.e.

$$V_{\mathrm{total}} = V_{\mathrm{ion-solvent}} + V_{\mathrm{solvent-solvent}} \tag{1}$$

The first term represents the interaction between the ion and the solvent and the second term is the pairwise intermolecular potential between solvent molecules. Briefly, the interaction potential describes each solvent molecule by six Lennard-Jones sites located at the atomic centers, and the acetonitrile dipole moment is represented by three partial charges placed on the nitrogen (−0.43), central carbon (+0.28), and methyl carbon (+0.15). The $[Os(bpy)_3]^{2+}$ complex is represented by a Lennard-Jones sphere with a +2 charge located at its center. The sphere and 504 solvent molecules were placed in a box with periodic boundary conditions. Classical trajectories were calculated with the AMBER molecular simulation package. Trajectories at constant pressure and temperature were run for 2.8 ns, with the first 1.4 ns being used to establish equilibrium and the latter 1.4 ns used to sample the solvent configurations.

The degree of solvent inhomogeneity is ascertained by comparing the electrostatic potential produced by the solvent at each of the three bipyridine ligands and the metal center. For the ligands, the potential is sampled over three points situated within the π-framework to account for the spatial extent of the MLCT charge distribution. For each configuration of the solvent we calculate the quantity

$$\Delta E_j = (3U_{\mathrm{M}} - U_j) - 2U_{\mathrm{M}} \tag{2}$$

where U_j and U_{M} are the electrostatic potentials observed at the jth ligand and the metal center, respectively. The first term (in parentheses) is the excited-state solvation energy for the case where the photoexcited electron is promoted to the jth ligand while keeping the solvent frozen in a configuration appropriate for the ground electronic state. The second term is the solvation energy of the ground state, and thus ΔE_j is the change in solvation energy that is associated with moving an electron from the metal center to the jth ligand. Figure 2 shows the distributions for the largest and smallest energy gaps. Energy differences in excess of 550 cm^{-1} are observed in approximately 65−70% of the ensemble. This suggests that while the majority of systems have localized excited states, there is still a substantial fraction of the ensemble in which the excited state is delocalized over two or more ligands at the instant of photon absorption, in accord with our previous conclusion. The simulations also suggest that the solvent induces an energy separation that is on average 2500 cm^{-1} between the lowest energy ligand and highest energy ligand, a value that is comparable to the spectral width of the triplet absorption band.

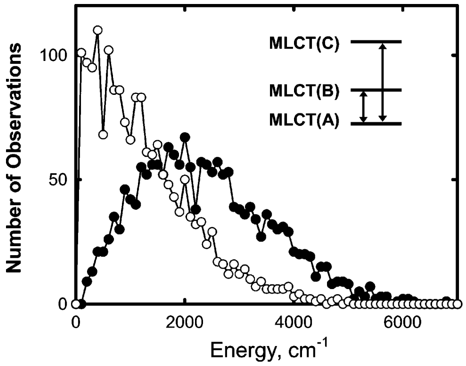

Figure 2. Distributions in the solvent induced energy splitting between ligands. Open circles show the smallest energy gap, and solid circles show the largest. The inset represents the energies of the three bipyridine ligands: MLCT(A) is the ligand with the lowest energy solvent configuration (i.e. the best solvated); MLCT(C) is the ligand with the highest energy solvent configuration; and MLCT(B) is intermediate.

Complexes residing in highly asymmetric solvent environments will exhibit three separate optical transitions. Photoexcitation at the red edge of the absorption band places the electron on the lowest energy ligand, i.e. the one with the most favorable solvent configuration. Excitations to the ligands with less favorable solvent configurations occur at higher energy. If the average value of the largest gap is 2500 cm^{-1}, then excitation to the highest energy ligand in the *triplet* absorption band would be in the vicinity of 600 nm, the blue edge. Because the solvent is not positioned appropriately for this MLCT charge distribution, it will rapidly reorganize. Thus, at higher photon energies, excess excitation energy could be directly placed into the solvent, rather than into molecular vibrations. The implications of this are discussed further in Section C.

B. Transient Absorption Studies. The excited-state dynamics are initiated by photoexcitation of $[Os(bpy)_3]^{2+}$ to a MLCT state with a femtosecond laser pulse and probed through a ligand-localized $\pi-\pi$* transition on the bipyridine radical anion (bpy^-) that is centered at 370 nm. The experiments described in this paper focus on both the changes in the *magic angle amplitude*, A_{MA}, and the *absorption anisotropy*, $r(t)$, of the excited-state absorptions. In this work, both of these quantities are derived from the transient spectra obtained with parallel and perpendicular pump−probe polarization conditions., i.e.

$$A_{\mathrm{MA}} = \frac{1}{3}(A_{\parallel} + 2A_{\perp}) \tag{3}$$

$$r(t) = \frac{A_{\parallel} - A_{\perp}}{A_{\parallel} + 2A_{\perp}} \tag{4}$$

The magic angle signal reflects changes in the shape of the excited-state absorption band (e.g. due to changes in population),

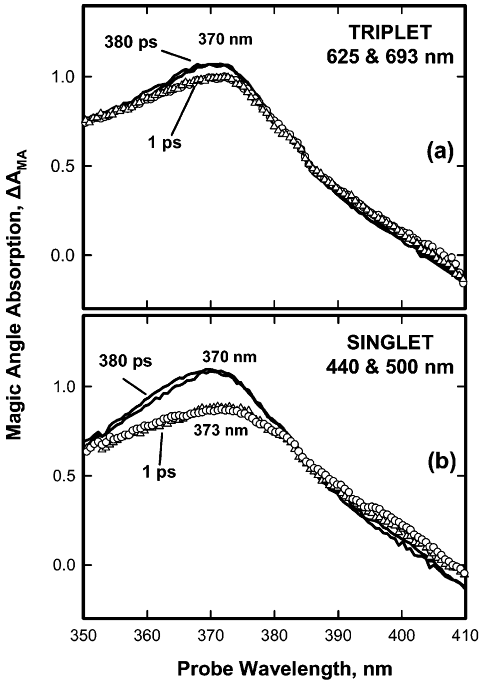

Figure 3. Magic angle transient absorption spectra (ΔA_{MA}) observed at 380 (—) and 1 ps (Δ, ○) after photoexcitation of $[Os(bpy)_3]^{2+}$ in room temperature acetonitrile: (a) spectra for ^{3}MLCT excitation and (b) spectra for ^{1}MLCT excitation.

while the anisotropy reflects changes in the transition dipole direction. Processes that alter the orientational distribution of the probe transition dipoles will lead to a decay in the magnitude of $r(t)$. In molecular systems rotational diffusion is the most common mechanism.

In the MLCT excited state of $[Os(bpy)_3]^{2+}$, ILET will also alter the direction of the probe transition dipole, and hence contribute to the anisotropy decay. The MLCT excitations are polarized along the metal−ligand axes, as long as the environmental heterogeneity is great enough to produce localized excited states, and the probe transition dipole is oriented along the long axis of the bipyridine ligand.[37] Because the pump and probe transition dipoles are orthogonal to each other, stronger excited-state absorption is observed when the probe beam is polarized perpendicular to that of the pump beam. From eq 4 it follows that the initial anisotropy value is negative, but with increasing time the system evolves to an isotropic one where the final anisotropy value is zero.

1. Magic Angle. Magic angle transient absorption spectra obtained at four different excitation wavelengths are displayed in Figure 3. Two spectra are shown for each excitation wavelength, one obtained at 1 ps and the other at 380 ps after photoexcitation. For clarity we present the data in two plots. The upper panel depicts the magic angle spectra resulting from ^{3}MLCT excitation (625 and 693 nm), while the lower one shows the magic angle spectra for ^{1}MLCT excitation (440 and 500 nm). The evolution of the spectra between these two temporal extremes is depicted in the contour plots shown in Figure 4, which show the transient absorption intensity as a function of both the pump−probe delay (y-axis) and probe wavelength (x-axis). Pump−probe delay (y-axis) is given on a logarithmic scale to permit inclusion of all transient spectra.

When the complex is excited in the triplet absorption band, only a slight evolution of the excited-state spectrum is observed. For both the 693 and 625 nm data, there is a small (∼5−6%) growth of intensity at the peak of the $\pi-\pi^*$ absorption from 1 (Δ and ○) to 380 ps (—). Additionally, there is a slight decay of intensity toward the red edge of the absorption (∼385 to 410 nm). In the plots shown in Figure 4a,b, a fast (<1 ps) growth of the absorption is the only discernible evolution of these two surfaces. This is also the case for each of the triplet excitation wavelengths studied (625, 650, 675, and 693 nm).

By contrast, the ^{1}MLCT excitations in Figure 3b exhibit a significant blue shift, as well as a large (∼25−30%) growth of signal intensity at the peak of the $\pi-\pi^*$ absorption. The transient spectra at 1 ps for the 500 (Δ) and 440 nm (○) excitations have a peak of the $\pi-\pi^*$ absorption centered at 373 nm. In the 380 ps limiting spectra (—), the peak of the absorption has shifted to 370 nm and the band has noticeably narrowed. This reshaping of the transient spectra takes place during the first 30−45 ps after photoexcitation (Figure 4c,d). Kinetic analysis reveals two time components. The fast time component is comparable to the subpicosecond evolution observed following triplet excitation. Since this fast evolution is observed at all excitation wavelengths, it is reasonable to assume that it stems from a common source, although its exact origin is at the moment unclear. The slow time component is observed only for the two singlet excitations, and is approximately 16 ps. While both the 500 and 440 nm excitations exhibit similar time scales, the *degree* of spectral shift differs. Difference spectra obtained by subtracting the 380 ps limiting spectrum from the 3.5 ps spectrum are shown in Figure 5 for each of the photoexcitation wavelengths. The difference spectra at 3.5 ps are chosen because by this time the fast (<1 ps) evolution is over and only the slow changes are evident. Both of the singlet excitations show significant spectral changes and the higher energy excitation (440 nm) seems to exhibit a slightly greater change than the lower energy excitation (500 nm).

One plausible interpretation of this observation is that the spectral blue shift is a signature of intersystem crossing in $[Os(bpy)_3]^{2+}$. If this were correct, it would make the ISC time in $[Os(bpy)_3]^{2+}$ about 100 times slower than the time scale measured in $[Ru(bpy)_3]^{2+}$. The spin−orbit coupling in $[Os(bpy)_3]^{2+}$ is even stronger than that in $[Ru(bpy)_3]^{2+}$ and since there is no significant structural rearrangement in the MLCT excited states, it is difficult to imagine why the ISC should be any slower in $[Os(bpy)_3]^{2+}$. In addition, one would anticipate that if it were the result of ISC, the magnitude of the spectral shift would be independent of the excitation wavelength within the ^{1}MLCT absorption band, which is contrary to our observations of a narrowing and blue shift of the spectrum.

On the other hand, these effects are consistent with vibrational energy relaxation (VER). In solution, VER can be described as a sequence of two processes: intramolecular vibrational redistribution (IVR) followed by a transfer of vibrational energy to the solvent (vibrational cooling). Although the order of events is well established, there is some ambiguity in the literature as to the time scales for IVR and vibrational cooling in large molecules (>25−30 atoms) dissolved in solution. For *trans*-stilbene, IVR is assigned to be as fast (or faster than) as 100 fs followed by cooling to the solvent in 8.5 ps.[38] In a variety of both free base and metalated porphyrins, IVR is generally given a time scale of ∼1 ps while vibrational cooling is ∼10−20 ps.[39−43] In their studies of *fac*-$[Re(MQ^+)(CO)_3(dmb)]^{2+}$ (where dmb = 4,4′-dimethyl-2,2′-bipyridine and MQ^+ = *N*-methyl-4,4′-bipyridinium) Vlček and co-workers describe complicated VER occurring in association with ILET.[44] In the same work, they also assign a time scale of ∼15 ps to vibrational cooling of $[Re(Etpy)(CO)_3(dmb)]^+$ (where Etpy = 4-ethylpyridine) in acetonitrile. In particular, Mizutani et al.[41] contribute a significant interpretation to the subject of VER for molecules in

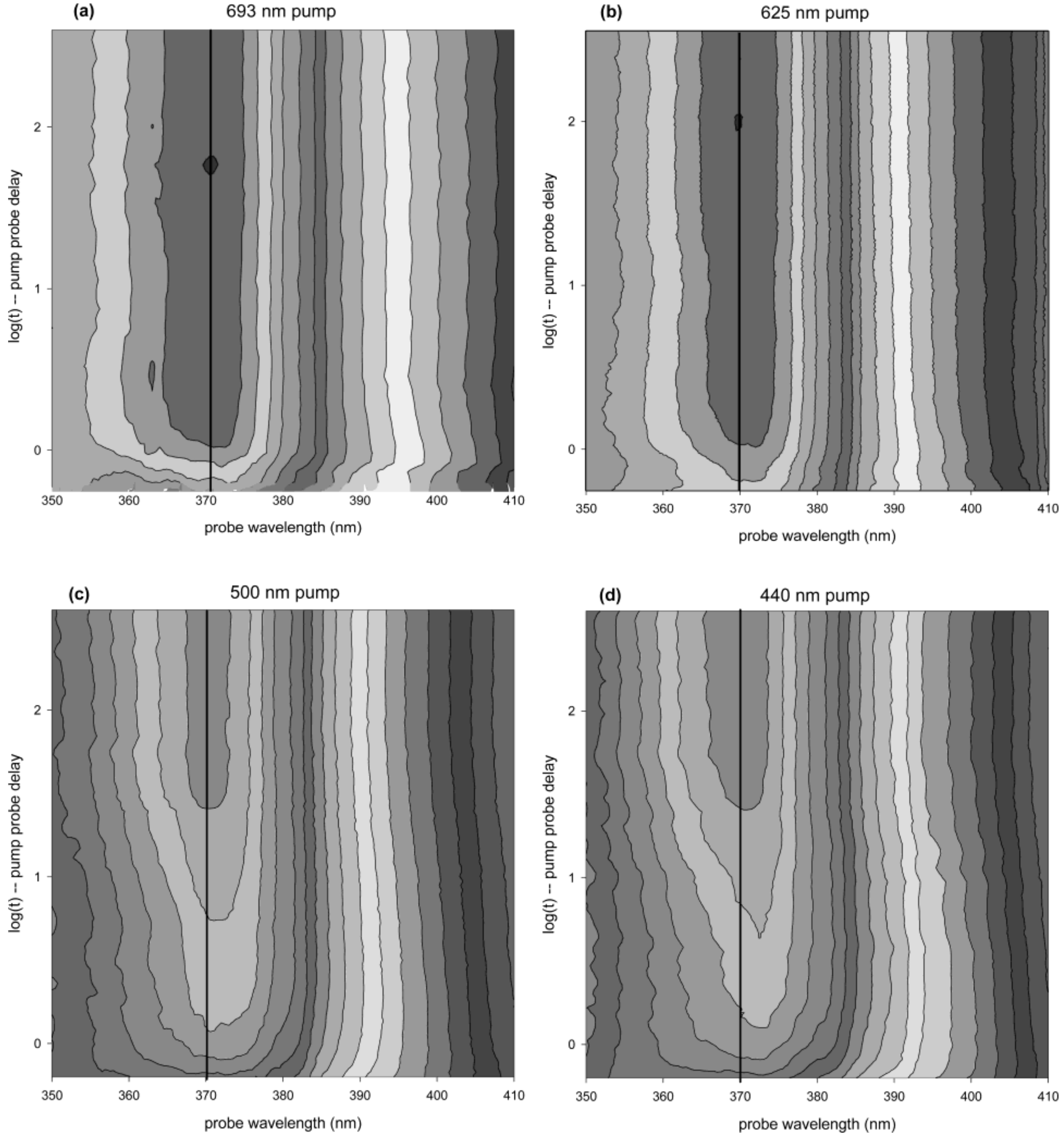

Figure 4. Magic angle transient absorption contour surface plots for ^{1}MLCT and ^{3}MLCT excitations. Surfaces correspond to excitation at (a) 693, (b) 625, (c) 500, and (d) 440 nm. A blue shift of the absorption band maximum is noticeable for panels c and d and absent for panels a and b.

solution as they reaffirm Vanden Bout et al.[45] by noting that the solvent provides the coupling and environment that assists IVR. This really blurs the distinction between the two processes involved in the VER path, especially in our case because it is through solvent fluctuations that the energies of the ligands are brought into resonance so that ILET can occur. Absorption band narrowing in transient absorption spectra has often been interpreted as vibrational cooling.[46] The amount of growth (25% of the total signal), the duration of the spectral evolution displayed (16 ps), and the dependence on excitation energy are all consistent with vibrational cooling observed in other large molecules dissolved in acetonitrile.[38,44] Thus, we assign the 16 ps component to vibrational cooling that occurs *after* a fast, subpicosecond, ISC event. In other words, it is cooling of a vibrationally hot *triplet* state.

In contrast to the 440 and 500 nm data, the triplet difference spectra (also shown in the figure) show no appreciable evolution

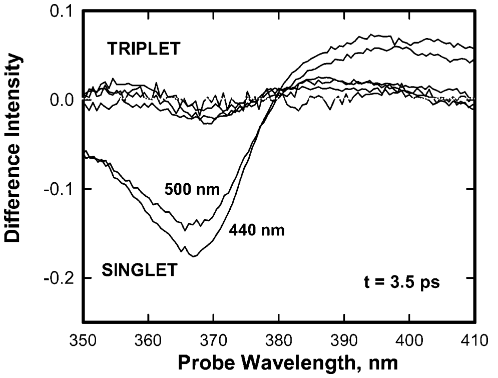

Figure 5. Difference spectra for ^{3}MLCT (693, 675, 650, and 625 nm) and ^{1}MLCT (500 and 440 nm) excitations obtained by subtracting the 380 ps limiting transient spectrum from the 3.5 ps transient spectrum.

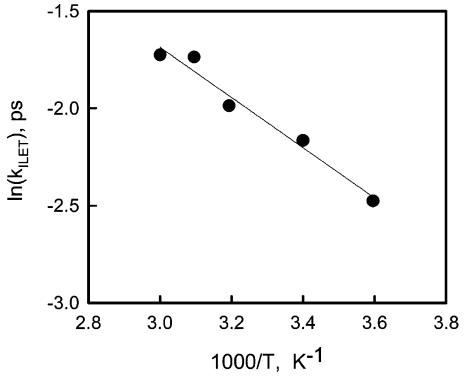

Figure 6. ILET rate constants as a function of temperature for $Os(bpy)_3^{2+}$ in acetonitrile.

after 3.5 ps, suggesting that vibrationally cold complexes are produced, even when the complex is excited at the blue edge of its absorption band (580 nm). This is discussed further in Section C.

2. Absorption Anisotropy. In a recent paper from our laboratory[35] we discussed absorption anisotropy measurements that assign the time scales for the ILET process in $[Os(bpy)_3]^{2+}$ and a mixed ligand osmium complex in acetonitrile and ethylene glycol. In that work, $[Os(bpy)_3]^{2+}$ was excited at the red edge of the ground state absorption spectrum (693 nm). Analysis of the anisotropy amplitudes suggests that photon absorption produces a distribution of excited state wave functions. For a majority of the ensemble, the excited state is localized on a single ligand, indicating that the solvent inhomogeneity is capable of overcoming the ligand−ligand electronic coupling. While this observation is at least qualitatively consistent with conventional thought, our experiments also suggest that in a sizable fraction (∼35−40%) of the ensemble the excited state is delocalized over two or more of the ligands.

In this work, we have measured the ILET rate as a function of temperature, which provides an estimate of the electron-transfer activation energy and electronic coupling. In addition, we have extended the anisotropy measurements to other excitation wavelengths. When these results are combined with the magic angle data presented in the previous section, a dynamical picture emerges that describes the evolution of the excited state following photoexcitation into both the singlet and triplet absorption bands.

a. Temperature Dependence. We have performed absorption anisotropy measurements with 693 nm excitation light at a series of temperatures and the results are displayed in Figure 6. From the slope, we obtain an activation enthalpy of 850 cm^{-1}. This represents the first direct measurement of the ILET barrier height in a polypyridyl complex.

The activation energy is related to the driving force (ΔG°), solvent reorganization energy (λ), and the electronic coupling between the ligands in the MLCT excited state (H_{el}), using an equation developed by Brunschwig and Sutin:[47]

$$\Delta G^* = \frac{\lambda}{4} + \frac{\Delta G^\circ}{2} + \frac{(\Delta G^\circ)^2}{4(\lambda - 2H_{el})} - H_{el} + \frac{{H_{el}}^2}{\lambda + \Delta G^\circ} \qquad (5)$$

λ has both inner- and outer-sphere contributions, i.e. $\lambda = (\lambda_I + \lambda_O)$. The inner-sphere contribution is approximated to be twice the reorganization energy associated with the MLCT excitation, i.e. $2\lambda_I^{MLCT}$, which can be determined from emission spectral fitting.[48] The factor of 2 arises because vibrational modes on two of the ligands are affected in the ILET process. We thus estimate $\lambda_I \approx 2000\ cm^{-1}$. The outer-sphere contribution is estimated from dielectric continuum models[49] to be about 2500−3000 cm^{-1}. Taking $\Delta G^\circ = 0$ for the symmetric ET process, $\lambda = (\lambda_I + \lambda_O) = 4500\ cm^{-1}$, and assuming that the activation entropy is small (i.e., $\Delta G^* \approx \Delta H^*$), we estimate H_{el} to be around 300−400 cm^{-1}.

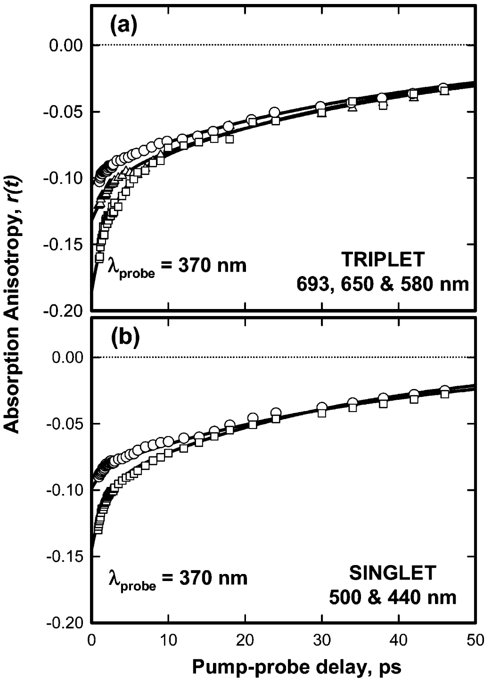

Figure 7. Absorption anisotropy decays at 370 nm for $[Os(bpy)_3]^{2+}$ in room temperature acetonitrile. The upper panel (a) shows transients for excitation into the ^{3}MLCT state: 693 (□), 650 (△), and 580 nm (○). The lower panel (b) shows transients for excitation into ^{1}MLCT state: 500 (□) and 440 nm (○). The solid lines are the result of biexponential to the data.

b. Pump-Wavelength-Dependent Decay Kinetics. Displayed in Figure 7 are anisotropy decays at 370 nm for $[Os(bpy)_3]^{2+}$ in acetonitrile. The upper panel shows $r(t)$ following triplet excitations (693, 650, and 580 nm) while the lower one shows the $r(t)$ following singlet excitations (500 and 440 nm). The most striking trend observed in this series of decays is the change in amplitude of the fast component. As the excitation wavelength is moved to the blue of 693 nm, the fast component gradually diminishes and by 580 nm it is nearly gone. It then reappears at the red edge of the singlet absorption band (500 nm), and again decreases as the excitation wavelength is shifted to higher energy.

The solid lines in Figure 7 are the results of biexponential fits for each data set. The time constants for the fast and slow kinetic components are given in Table 1. (Note that the anisotropy decays at 625 and 675 nm are not shown in the figure.) The slow component is attributed to rotational diffusion, and is relatively independent of excitation wavelength, both in its time constant (∼40 ps) and its amplitude. These results are consistent with our previously published results for $[Os(bpy)_3]^{2+}$.[35] The fast component of the decay is assigned to ILET. The ∼3 ps time scale observed at the 693, 675, and 650 nm excitations also agrees with our previous work.[35] For the other two triplet excitations (625 and 580 nm), the time constant obtained from the biexponential fit is likely an average of a component much faster than 1 ps and a slower one of approximately 3 ps. A more quantitative measure of these two "fast" components is hampered by a decrease in amplitude at these wavelengths. The 500 nm singlet excitation has a fast time component of 1.5 ps, about twice as fast as the lowest energy

TABLE 1: Summary of Fast and Slow Time Constants Resulting from Biexponential Fits of the Absorption Anisotropy Decays, $r(t)$[a]

	excitation wavelength, nm						
	693	675	650	625	580	500	440
fast component (ps)	2.8	3.0	3.1	2.5[b]	1.2[b]	1.5	0.7[b]
slow component (ps)	41	41	42	41	38	33	39

[a] Nonlinear least-squares analysis revealed that the $r(t)$ transients at a probe wavelength of 370 nm (the peak of the $\pi-\pi^*$ absorption) exhibit biphasic kinetics for all excitations. [b] Our kinetic analysis suggests that these are most likely an average of two kinetic components, a fast one that could not be resolved ($\ll$1 ps) and a slower one ($\approx$3 ps for 625 and 580 nm excitations and $\approx$1.5−2 ps for the 440 nm excitation).

triplet excitations. Like the blue triplet excitations, the fast component in the 440 nm decay also appears to be a combination of two subcomponents.

c. Anisotropy Amplitudes. The initial amplitude of the absorption anisotropy can provide details regarding the symmetry of the optically prepared excited state. For an initially *localized* excited state, the pump and probe transition dipoles are orthogonal to each other, and the excited-state absorption band will have $r(t=0) = -0.2$. If the wave function of the initial state is delocalized, on the other hand, then $r(t=0) = -0.1$. Thus, the value of $r(t=0)$ provides a measure of the degree of localization in the optically prepared excited state.

Obtaining the initial anisotropy amplitude from a transient absorption experiment is not necessarily straightforward,[34,35] since the observed absorption anisotropy is a weighted average of the *absorption* and *bleach* anisotropies, $\langle r_\alpha(t)\rangle$ and $\langle r_\beta(t)\rangle$, respectively. The observed anisotropy is given by

$$r(t) = \frac{\alpha^{\mathrm{T}}}{\alpha^{\mathrm{T}} - \beta^{\mathrm{T}}}\langle r_\alpha(t)\rangle - \frac{\beta^{\mathrm{T}}}{\alpha^{\mathrm{T}} - \beta^{\mathrm{T}}}\langle r_\beta(t)\rangle \qquad (6)$$

where α^{T} and β^{T} are the total absorption and total bleach contributions, respectively (both are positive quantities). We have developed a procedure for modeling the anisotropy data of $[\mathrm{Os(bpy)_3}]^{2+}$, the details of which are discussed elsewhere.[35] But briefly, we use eq 6 to simultaneously fit the observed $r(t)$ transient data at seven probe wavelengths (360, 370, 375, 380, 385, 390, and 395 nm) across the $\pi-\pi^*$ absorption band. From the analysis we extract the *absorption* anisotropy, $\langle r_\alpha(t)\rangle$, which has the following form:

$$\langle r_\alpha(t)\rangle = a_{\mathrm{F}}^{\lambda}\exp(-k_{\mathrm{F}}t) + a_{\mathrm{S}}^{\lambda}\exp(-k_{\mathrm{S}}t) \qquad (7)$$

The time constants (k_{F} and k_{S}) are for the fast and slow components of the decay, respectively. The related amplitudes (a_{F}^{λ} and a_{S}^{λ}) are both equal to −0.1 when the initial wave function is localized on a single ligand, and then randomizes among the three ligands through ILET.

The values of a_{F}^{λ} and a_{S}^{λ} at each excitation wavelength are plotted in Figure 8. The gray bands that accompany the amplitudes reflect the uncertainty in the values obtained from the model. Regardless of excitation wavelength, the amplitudes of the slow component (a_{S}^{λ}) are ca. −0.1, which is the value expected once the photoexcited electron scrambles among the three ligands through ILET. The fast amplitude reflects the nature of the *initial* state, and unlike the slow component, the fast component exhibits a strong dependence on excitation wavelength, indicating that the nature of the excited-state wave function depends on the color of the photon absorbed. Localized states would have fast amplitudes (a_{F}^{λ}) equal to −0.1, while for excited states delocalized over all three ligands a_{F}^{λ} would be zero. When the complex is excited at the red edge of the ^{3}MLCT absorption band, the initial anisotropy ($a_{\mathrm{F}}^{\lambda} + a_{\mathrm{S}}^{\lambda}$) is between −0.1 and −0.2, indicating that there is a mixture of localized and delocalized excited states in the initial ensemble.

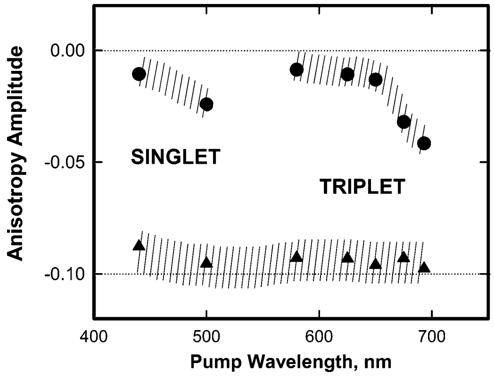

Figure 8. Initial absorption anisotropy amplitudes as a function of pump wavelength for $[\mathrm{Os(bpy)_3}]^{2+}$. The solid circles (●) and triangles (▲) correspond to the initial amplitudes of the fast and slow components of eq 7 (a_{F}^{λ} and a_{S}^{λ}), respectively. The hatching that accompanies the amplitudes represents the uncertainty range associated with the modeling. The values for a_{F}^{λ} are all less than −0.1, which suggests differing degrees of initial excited-state delocalization with a strong dependence on excitation wavelength. The values for a_{S}^{λ} are $\approx$ −0.1, which is the expected value after the electron randomizes through ILET.

C. Excited-State Evolution. Regardless of the color of light used to excite the molecules, the agreement of the four 380 ps magic angle spectra in Figure 3 indicates that at long times after photoexcitation the system ultimately resides in the same low-energy triplet state. However, the path taken to arrive in this state is very dependent on excitation wavelength. The transient spectra that result from excitation to the triplet state exhibit one type of behavior, while the transient spectra observed after singlet excitation show something very different (Section B1). Thus, any description of the excited-state evolution must distinguish direct population of the triplet state from the triplet state formed after intersystem crossing from the singlet. Four distinct scenarios are considered: (1) low-energy excitation in the ^{3}MLCT band, (2) high-energy excitation of the triplet, (3) low-energy excitation of the singlet, and (4) high-energy excitation of the singlet. These four transitions are summarized in Figure 9.

The MLCT excited states consist of multiple minima that correspond to locating the photoexcited electron on each of the ligands. For clarity, only two minima are shown in the figure; however, in reality three exist. A three-dimensional view of this surface is shown in our previous paper. The point where the two diabatic curves cross corresponds to the solvent configuration that brings (at least) two of the ligands into resonance, and because of the ligand−ligand coupling the localized basis states are mixed to form two delocalized states. Because of the strong ligand−ligand electronic coupling in this system, the diabatic surfaces undergo an avoided crossing to form the adiabatic surfaces depicted in the figure. It is worth noting that Kelley and co-workers[50,51] examined the ILET process in $[\mathrm{Os(bpy)_3}]^{2+}$ via absorption anisotropy measurements. Although the time resolution of their apparatus was limited to 10 ps, they concluded that $[\mathrm{Os(bpy)_3}]^{2+}$ ILET dynamics in acetonitrile take place on a 130 ps time scale and occur in a nonadiabatic coupling limit.[50,51] These findings are in direct contrast to our observations.

1. Low-Energy ^{3}MLCT Excitation. When the $[\mathrm{Os(bpy)_3}]^{2+}$ complex is excited at the red edge (693 nm) of its triplet band,

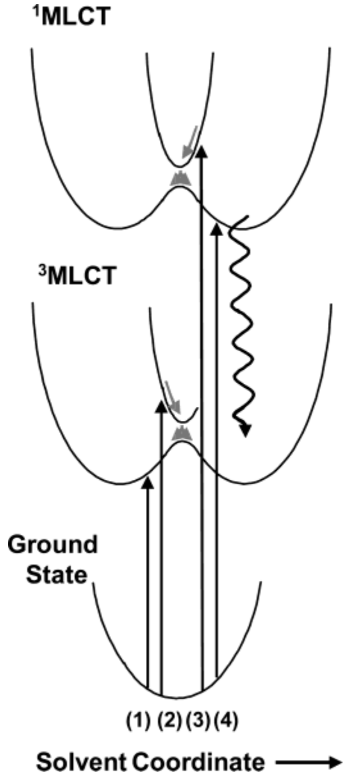

Figure 9. Schematic potential energy surfaces for the $[Os(bpy)_3]^{2+}$ ground state, ^{3}MLCT state, and ^{1}MLCT state in polar solvents. The MLCT excited states are represented by adiabatic surfaces formed from the avoided crossing of potential wells that correspond to the localization of the photoexcited electron on a different ligand. The actual surface would possess three wells, while for clarity, only two are shown here. The four transitions labeled (1)−(4) correspond to the different types of transitions explored in this work. See text for details.

the initial anisotropy is −0.14, which indicates that the excited ensemble consists of both localized and delocalized excited states. While some fraction of the ensemble is delocalized over two or more of the ligands, most of the population starts out on the lowest three-dimensional surface in Figure 9, in a localized region of the parabolic potential. The time scale for movement of the excited state from one parabolic surface to another (i.e. ILET) is equal to $1/3(k_{obs} - k_{rot})$, where k_{obs} is the observed decay rate (fast component) and k_{rot} is the rotational diffusion rate (slow component), i.e., $k_{obs} = (3k_{ILET} + k_{rot})$. Using the kinetic rates presented in Table 1 yields an ILET time of ≈9 ps.

2. High-Energy ^{3}MLCT Excitation. Excitations at 625 and 580 nm show qualitatively different anisotropy behavior. Both exhibit initial anisotropy values in the neighborhood of −0.11. The time scale of the fast component is also different, and as stated earlier, both wavelengths show some evidence of a fast (<1 ps) decay time. Both observations are consistent with an initial state starting on the upper adiabatic surface instead of the lowest one. In such a case, the excited state would initially be localized, then quickly delocalize over two ligands as it approached the avoided crossing from above.

The differences between these potential surfaces in Figure 9 correspond to the different solvent configurations around each ligand. When excited to the higher energy surface, the MLCT excitation is placed on a ligand with a less than favorable solvent configuration around it. Thus, as the excitation energy is increased, the excess energy is placed in the solvent degrees of freedom rather than molecular vibrations. Our molecular dynamics simulations support the notion that in the average solvent configuration the energy difference between the best solvated and worst solvated ligands is about 2500 cm^{-1}, nearly the entire width of the ^{3}MLCT absorption band. By promoting the electron to a less-solvated ligand (i.e. upper adiabatic surface) the complex would remain vibrationally cold and this would explain the lack of evolution in the magic angle spectra.

3. Low-Energy ^{1}MLCT Excitation. Following photoexcitation at 500 nm, the complex undergoes rapid ISC to the triplet state, with the MLCT excitation remaining on the ligand to which the electron was initially excited. The ISC process produces a vibrationally hot triplet state, which then cools through energy transfer to the solvent (16 ps). As this state cools, it undergoes ILET events with an electron transfer time of 4.5 ps (1.5 ps anisotropy decay), which is consistent with the expectation that ILET should proceed more quickly with the introduction of excess vibrational energy.

4. High-Energy ^{1}MLCT Excitation. At 440 nm excitation, the complex is promoted to one of the upper Marcus surfaces in the *singlet* state, which would lead to rapid delocalization as the system approached the avoided crossing from above. As occurs in the 500 nm excitation, ISC yields a vibrationally hot triplet state that reaches thermal equilibrium with the solvent on a 16 ps time scale.

Acknowledgment. Funding for this project was provided by The Research Corporation (RI0048), the Petroleum Research Fund (36385-G6), and the National Science Foundation (CHE-0301266). The authors also acknowledge a number of discussions with Thomas J. Meyer at Los Alamos National Laboratory.

References and Notes

(1) Demas, J. N.; Crosby, G. A. *J. Am. Chem. Soc.* **1971**, *93*, 2841−2847.
(2) Van Houten, J.; Watts, R. J. *J. Am. Chem. Soc.* **1976**, *98*, 4853.
(3) Van Houten, J.; Watts, R. J. *Inorg. Chem.* **1978**, *17*, 3381.
(4) Vlcek, A. *Coord. Chem. Rev.* **2000**, *200*, 933−977.
(5) Lumpkin, R. S.; Kober, E. M.; Worl, L. A.; Murtaza, Z.; Meyer, T. J. *J. Phys. Chem.* **1990**, *94*, 239−243.
(6) Meyer, T. J. *Pure Appl. Chem.* **1986**, *58*, 1193−1206.
(7) Caspar, J. V.; Westmoreland, T. D.; Allen, G. H.; Bradley, P. G.; Meyer, T. J.; Woodruff, W. H. *J. Am. Chem. Soc.* **1984**, *106*, 3492−3500.
(8) Durham, B.; Caspar, J. V.; Nagle, J. K.; Meyer, T. J. *J. Am. Chem. Soc.* **1982**, *104*, 4803−4810.
(9) Creutz, C.; Chou, M.; Netzel, T. L.; Okumura, M.; Sutin, N. *J. Am. Chem. Soc.* **1980**, *102*, 1309−1319.
(10) Kuciauskas, D.; Freund, M. S.; Gray, H. B.; Winkler, J. R.; Lewis, N. S. *J. Phys. Chem. B* **2001**, *105*, 392−403.
(11) Schwarz, O.; Van Loyen, D.; Jockusch, S.; Turro, N. J.; Durr, H. *J. Photochem. Photobiol., A* **2000**, *132*, 91−98.
(12) Kohle, O.; Ruile, S.; Gratzel, M. *Inorg. Chem.* **1996**, *35*, 4779−4787.
(13) Albano, G.; Belser, P.; Daul, C. *Inorg. Chem.* **2001**, *40*, 1408−1413.
(14) Belser, P.; Bernhard, S.; Blum, C.; Beyeler, A.; De Cola, L.; Balzani, V. *Coord. Chem. Rev.* **1999**, *192*, 155−169.
(15) Kalyanasundaram, K.; Gratzel, M. *Coord. Chem. Rev.* **1998**, *177*, 347−414.
(16) Launay, J. P.; Fraysse, S.; Coudret, C. *Mol. Cryst. Liq. Cryst.* **2000**, *344*, 125−132.
(17) Harriman, A.; Ziessel, R. *Coord. Chem. Rev.* **1998**, *171*, 331−339.
(18) Damrauer, N. H.; Cerullo, G.; Yeh, A.; Boussie, T. R.; Shank, C. V.; Mccusker, J. K. *Science* **1997**, *275*, 54−57.
(19) Bhasikuttan, A. C.; Suzuki, M.; Nakashima, S.; Okada, T. *J. Am. Chem. Soc.* **2002**, *124*, 8398−8405.
(20) Browne, W. R.; Coates, C. G.; Brady, C.; Matousek, P.; Towrie, M.; Botchway, S. W.; Parker, A. W.; Vos, J. G.; Mcgarvey, J. J. *J. Am. Chem. Soc.* **2003**, *125*, 1706−1707.
(21) Mabrouk, P. A.; Wrighton, M. S. *Inorg. Chem.* **1986**, *25*, 526−531.
(22) Bradley, P. G.; Kress, N.; Hornberger, B. A.; Dallinger, R. F.; Woodruff, W. H. *J. Am. Chem. Soc.* **1981**, *103*, 7441−7446.

(23) Riesen, H.; Wallace, L.; Krausz, E. *Inorg. Chem.* **2000**, *39*, 5044−5052.

(24) Yersin, H.; Strasser, J. *Coord. Chem. Rev.* **2000**, *208*, 331−364.

(25) Yersin, H.; Humbs, W. *Inorg. Chem.* **1999**, *38*, 5820−5831.

(26) Riesen, H.; Krausz, E. *Chem. Phys. Lett.* **1998**, *287*, 388−394.

(27) Riesen, H.; Wallace, L.; Krausz, E. *Int. Rev. Phys. Chem.* **1997**, *16*, 291−359.

(28) Karki, L.; Hupp, J. T. *Inorg. Chem.* **1997**, *36*, 3318−3321.

(29) Humbs, W.; Strasser, J.; Yersin, H. *J. Lumin.* **1997**, *72−4*, 677−678.

(30) Riesen, H.; Wallace, L.; Krausz, E. *J. Chem. Phys.* **1995**, *102*, 4823−4831.

(31) Huber, P.; Yersin, H. *J. Phys. Chem.* **1993**, *97*, 12705−12709.

(32) Oh, D. H.; Boxer, S. G. *J. Am. Chem. Soc.* **1989**, *111*, 1130−1131.

(33) Kober, E. M.; Sullivan, B. P.; Meyer, T. J. *Inorg. Chem.* **1984**, *23*, 2098−2104.

(34) Yeh, A. T.; Shank, C. V.; McCusker, J. K. *Science* **2000**, *289*, 935−938.

(35) Shaw, G. B.; Brown, C. L.; Papanikolas, J. M. *J. Phys. Chem. A* **2002**, *106*, 1483−1495.

(36) Shaw, G. B.; Papanikolas, J. M. *J. Phys. Chem. B* **2002**, *106*, 6156−6162.

(37) König, E.; Kremer, S. *Chem. Phys. Lett.* **1970**, *5*, 87−90.

(38) Kovalenko, S. A.; Schanz, R.; Hennig, H.; Ernsting, N. P. *J. Chem. Phys.* **2001**, *115*, 3256−3273.

(39) Baskin, J. S.; Yu, H. Z.; Zewail, A. H. *J. Phys. Chem. A* **2002**, *106*, 9837−9844.

(40) Yu, H. Z.; Baskin, J. S.; Zewail, A. H. *J. Phys. Chem. A* **2002**, *106*, 9845−9854.

(41) Mizutani, Y.; Uesugi, Y.; Kitagawa, T. *J. Chem. Phys.* **1999**, *111*, 8950−8962.

(42) Yu, H. Z.; Baskin, J. S.; Steiger, B.; Wan, C. Z.; Anson, F. C.; Zewail, A. H. *Chem. Phys. Lett.* **1998**, *293*, 1−8.

(43) Eom, H. S.; Jeoung, S. C.; Kim, D.; Ha, J. H.; Kim, Y. R. *J. Phys. Chem. A* **1997**, *101*, 3661−3669.

(44) Liard, D. J.; Busby, M.; Farrell, I. R.; Matousek, P.; Towrie, M.; Vlček, A. *J. Phys. Chem. A* **2004**, *108*, 556−567.

(45) Vanden Bout, D.; Freitas, J. E.; Berg, M. *Chem. Phys. Lett.* **1994**, *229*, 87−92.

(46) Gustafson, T. L.; Kyllo, E. M.; Frost, T. L.; Sun, R. G.; Lim, H. S.; Wang, D. K.; Epstein, A. J.; Lefumeux, C.; Burdzinski, G.; Buntinx, G.; Poizat, O. *Synth. Met.* **2001**, *116*, 31−34.

(47) Brunschwig, B. S.; Sutin, N. *Coord. Chem. Rev.* **1999**, *187*, 233−254.

(48) Murtaza, Z.; Graff, D. K.; Zipp, A. P.; Worl, L. A.; Jones, W. E.; Bates, W. D.; Meyer, T. J. *J. Phys. Chem.* **1994**, *98*, 10504−10513.

(49) Brunschwig, B. S.; Ehrenson, S.; Sutin, N. *J. Phys. Chem.* **1987**, *91*, 4714−4723.

(50) Pogge, J. L.; Kelley, D. F. *Chem. Phys. Lett.* **1995**, *238*, 16−24.

(51) Cushing, J. P.; Butoi, C.; Kelley, D. F. *J. Phys. Chem. A* **1997**, *101*, 7222−7230.